This is the version of record of:

Ulian, Gianfranco, Moro, Daniele and Valdrè, Giovanni. "Thermodynamic and thermoelastic properties of wurtzite-ZnS by density functional theory" *American Mineralogist*, vol. 105, no. 8, 2020, pp. 1212-1222

The final publication is available at ***https://doi.org/10.2138/am-2020-7330***

Terms of use: All rights reserved.

This item was downloaded from IRIS Università di Bologna (https://cris.unibo.it/)

When citing, please refer to the published version.

American Mineralogist, Volume 105, pages 1212–1222, 2020

Thermodynamic and thermoelastic properties of wurtzite-ZnS by density functional theory

Gianfranco Ulian[1,†], Daniele Moro[1], and Giovanni Valdrè[1,*]

[1]Dipartimento di Scienze Biologiche, Geologiche e Ambientali, Centro di Ricerche Interdisciplinari di Biomineralogia, Cristallografia e Biomateriali, Università di Bologna "Alma Mater Studiorum" Piazza di Porta San Donato 1, 40126 Bologna, Italy

Abstract

In the present paper, we provide a detailed theoretical investigation on fundamental thermodynamic, thermomechanical, and electronic properties of wurtzite ZnS between 0–20 GPa and 0–2000 K, obtained by ab initio density functional theory and the B3LYP functional. Several properties, such as phonon dispersion relations, elastic and piezoelectric constants, and thermodynamic and thermoelastic behaviors were calculated and reported. The analysis of the data via volume-integrated third-order Birch-Murnaghan fitting resulted in $K_0 = 72.17(4)$ GPa, $K' = 3.87(1)$, and $V_0 = 85.781(1)$ Å^3 at $T = 0$ K. The Born criteria for the mechanical stability of the mineral phase showed that wurtzite is unstable above about 19 GPa in static conditions. We calculated a direct bandgap for wz-ZnS of 4.86 eV at zero compression, which became an indirect one by increasing pressure above 17 GPa. The results are in good agreement with the experimental and theoretical ones reported in the literature, and further extend the knowledge of an important zinc sulfide phase, for both geological and industrial applications.

Keywords: Wurtzite ZnS, thermodynamic properties, elastic properties, electronic properties, density functional theory, quasi-harmonic approximation

Introduction

Zinc sulfide ZnS belongs to the important family of the zinc monochalcogenides whose general formula is ZnX, with X = S, O, Se, Te, or Cd. All the ZnX phases are isostructural and, from the mineralogical point of view, zinc sulfide is commonly found either as zinc-blende (zb-ZnS, mineralogical name sphalerite) or wurtzite (wz-ZnS). Both of them have a closed-packed structure, but sphalerite belongs to the cubic system, with space group $F\bar{4}3m$ and cubic close packing ($3C$) with ABC sequence along <111> direction, whereas wz-ZnS has an hexagonal unit cell ($2H$) related to the space group $P6_3mc$ (Fig. 1) with AB stacking along the [001] direction (Frey et al. 1986). In both zb- and wz-ZnS phases, each ion, either Zn^{2+} or S^{2-}, has a tetrahedral coordination. The structural difference between the two polymorphs is attributed to the stacking order of crystal planes along one of the C_3 axes and, according to Cardona et al. (2010), explains their very small difference of the enthalpies of formation. In addition, wurtzite is a high-temperature phase with respect to sphalerite, with a two-step $3C \rightarrow 2H$ transition at a temperature of about 1280–1300 K (Frey et al. 1986). There exists a third, high-pressure polymorph of ZnS, characterized by a halite-like structure (NaCl), with octahedral coordination of the ions, which is called rock salt (rs) ZnS (space group $Fm\bar{3}m$).

In a very recent work we investigated in details by ab initio density functional theory (DFT) simulations the thermodynamic and thermoelastic behavior of both cubic polymorphs of ZnS, finding that the zinc-blende to rock-salt phase transition occurs at 14.3 GPa at ~300 K (Ulian and Valdrè 2019b), which was in very good agreement with the experimental result of Ono and Kikegawa (2018) in the same temperature condition (13.4 GPa).

The aim of the present paper is to extend the knowledge on the zinc sulfide polymorphs by providing thermodynamic, thermoelastic, and electronic properties of the wurtzite ZnS phase. Indeed, there is a continuous and still growing interest in its various and manifold applications. For example, zinc sulfide is an ore mineral, which is smelted to obtain zinc, and it is searched in the Earth crust by employing different approaches (Kowalczuk et al. 2018). One of them, which is increasingly used at a global scale, is based on three-dimensional reflection seismic methods that provide high-resolution (order of meters to tens of meters) deep-penetration data from about 300 m to 4 km (Malehmir et al. 2012; Bellefleur et al. 2015). A successful application of these methods requires detailed knowledge of the seismic wave propagation in the mineral structure, data that can be calculated from the elastic constant tensor.

In addition, wz-ZnS is the first discovered semiconductor and has very important and interesting electric/electrodynamic, mechanical, and thermodynamic properties for applications in optoelectronic devices (e.g., displays, photodetectors) and in micro- and nanoelectromechanical systems (Özgür et al. 2005; Sang et al. 2013; Wang et al. 2017; Kandpal and Gupta 2018; Ossai and Raghavan 2018; Sinha et al. 2018; Xu et al. 2018). It is then not a surprise that wurtzite shares its name to all isostructural semiconductors of II-IV type. The remarkable chemical and physical features of this mineral phase, e.g., a wide bandgap of about 3.87 eV (region of UV light), high optical transmittance of visible light, polar surfaces, piezoelectric behaviors, and good thermal stability, make wurtzite ZnS a highly valuable material (Cline et al. 1967; Adachi 2005; Xu et al. 2018).

For all these reasons, it is crucial to carefully investigate the

* E-mail: giovanni.valdre@unibo.it
† Orcid 0000-0002-9292-3077.

0003-004X/20/0008–1212$05.00/DOI: https://doi.org/10.2138/am-2020-7330

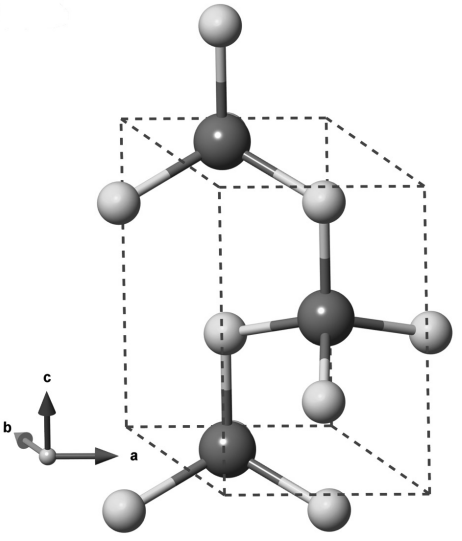

Figure 1. Wurtzite unit-cell model, with zinc and sulfur atoms colored in dark gray and light gray, respectively.

interplay of structural, elastic, thermodynamic, and electronic properties in zinc sulfide at different pressure and temperature conditions, in particular for the wurtzite phase. This kind of research is often experimentally challenging, because many features of the phase, for the sake of an example the piezoelectric constants, can be measured only from single crystals of wurtzite. Such samples, when not available in nature, are usually difficult and expensive to grow in the laboratory. In this context, ab initio theoretical simulations are a promising and well-established alternative, which can help the design of future experiments, e.g., aiding experimentalists to screen and select the most promising materials for crystal growth purposes (Catti et al. 2003).

Following these considerations, in the present work we present a detailed and comprehensive analysis of the cited properties of wurtzite, conducted by ab initio density functional theory simulations that follow and complete the one proposed in our previous work on sphalerite and rs-ZnS (Ulian and Valdrè 2019b). The aim is to provide a detailed set of data on several properties of wz-ZnS, obtained at the same level of theory to allow a direct and fruitful discussion on the polymorphs of zinc sulfide. Several aspects of wurtzite were investigated at the static (0 K) limit, and we included the temperature effects by employing the so-called *quasi-harmonic approximation* on the lattice dynamics. More into details, we provide (1) the geometry of wurtzite both at equilibrium and after hydrostatic deformation, (2) the equation of state (EoS) of the phase, (3) the electronic band structure and density of states, the second-order elastic constants, and the piezoelectric tensor, calculated as a function of applied pressure, and (4) the thermodynamic and thermoelastic behavior of wz-ZnS over the pressure and temperature range 0–20 GPa and 0–2000 K, respectively.

This paper is organized as follows. In the next section, the theory and algorithms used to calculate the above properties are briefly explained, providing the background of the work. Then, we present the obtained results, subdivided into a small subsection for each property, and discuss them with previous experimental and theoretical researches on wurtzite. Indeed, the properties of this mineral were previously simulated with several theoretical approaches, and we compared the effect of the computational parameters (basis set, Hamiltonians) on the calculated properties. Finally, we draw up the geological and technological implications of this work.

Computational methods

In the present work, we performed ab initio DFT simulations with the CRYSTAL17 code (Dovesi et al. 2018). Since we were interested in the mechanical and thermodynamic properties of wz-ZnS, we chose the B3LYP hybrid functional (Lee et al. 1988; Becke 1993a, 1993b) because of its well-known reliability with both structural and vibrational feature of solid systems (Ottonello et al. 2010; Prencipe et al. 2011; Belmonte et al. 2017). The description of the Zn and S orbitals is made via Gaussian-type functions, and we chose the Peitinger-Oliveira-Bredow (POB) double-ζ valence basis set with polarization (Peintinger et al. 2013; Ulian and Valdrè 2019b). We employed a pruned grid consisting of 75 points and 974 angular points to evaluate the exchange–correlation contribution by numerical integration of the electron density and its gradient over the volume of the unit cell. We set the tolerances for truncation of the Coulomb and exchange integrals to 10^{-7} and 10^{-16}, which means that when the overlap between two atomic orbitals is lower than the threshold, the corresponding integral is either discarded or treated with less precision. We diagonalized the Hamiltonian matrix at 50 k points in the reciprocal space by employing a 8 × 8 × 8 Monkhorst-Pack net (Monkhorst and Pack 1976).

Geometry optimization and equation of state

To calculate the equation of state of wurtzite at static conditions (0 K, no zero-point energy correction), we considered 11 unit-cell volumes in the range 0.82–1.12 V_0, with V_0 being the equilibrium geometry. We calculated the starting (equilibrium) geometry by optimizing the unit-cell parameters and the internal coordinates of the atoms at the same time, by employing a numerical gradient for the former and the analytical gradient method for the latter. The compressed and expanded unit cells for the equation of state were then optimized at constant volume by a symmetry preserving, variable cell-shape structure relaxation approach (Ottonello et al. 2010). For both equilibrium and hydrostatically deformed unit cell, the geometry optimization was considered converged when the gradient and the maximum atomic displacement were lower than 1×10^{-5} hartree bohr^{-1} and 4×10^{-5} bohr, respectively, with respect to the previous optimization step.

The equation of state of the mineral was calculated by fitting the unit-cell energy, E, as a function of the volume, V, using the volume-integrated third-order Birch-Murnaghan (Hebbache and Zemzemi 2004):

$$E = E_0 + \frac{9}{16} K_0 V_0 \left\{ K' \left(\eta^2 - 1\right)^3 + \left[\left(\eta^2 - 1\right)^2 \left(6 - 4\eta^2\right) \right] \right\} \quad (1)$$

with $\eta = (V_0/V)^{-1/3}$, K_0 is the bulk modulus of the system at both 0 GPa and 0 K, K' its pressure first derivative, and V_0 the volume at zero pressure (to be not confused with the volume of the unit cell at equilibrium). E_0 is the energy of the unit cell at zero pressure and temperature.

The pressure corresponding to the compression/expansion of the unit cell was calculated by using these parameters in the well-known $P(V)$ formulation of the BM3 (Birch 1947):

$$P = \frac{3}{2} K_0 \left[\eta^{-7/3} - \eta^{-5/3}\right] \left\{ 1 - \frac{3}{4} \left(4 - K'\right) \left(\eta^{-2/3} - 1\right) \right\} + P_0. \quad (2)$$

Second-order elastic moduli

The elastic moduli for any crystal are obtained from the analytical derivatives of the total energy as a function of crystal deformation. To this aim, we employed a fully automated procedure, which was implemented in the CRYSTAL code (Perger et al. 2009; Perger 2010). To remove the internal forces due to finite strain, the lattice parameters and the internal coordinates of the crystal are relaxed using analytic gradients (Doll 2001; Doll et al. 2001). In this work, the elastic moduli were calculated using seven points of displacement with a step of 0.005 Å. Since wurtzite has an hexagonal unit cell, the reference axis was oriented according to the guidelines of the Institute of Radio Engineering (IRE). In further details, during the simulations

the Cartesian x and z axes of the reference system were oriented along the **a** and **c** lattice vectors of the unit cell, respectively (Brainerd 1949).

We also performed the evaluation of the elastic moduli at different compressive states (*vide supra*). In this case, we employed a correction that considers the finite pre-stress $\sigma_{pre} = P\delta_{ij}$, imposed on the system (Barron and Klein 1965; Erba et al. 2014).

We calculated the single-crystal directional behavior of the elastic properties of wurtzite following the approach suggested by Marmier and coworkers (2010).

Since most materials are not single crystals, for practical applications we calculated also the polycrystalline elastic properties according to the formulations of both Nye (1957) and Voigt, Reuss, and Hill, VRH (Hill 1952). Pugh's ratio (k) and Vicker's hardness (H_V) were also calculated according to the formulation of Chen et al. (2011). The Pugh's ratio is a dimensionless empirical parameter, given by the ratio between the bulk (K) and the shear (μ) moduli, whose value represents an index of the ductile ($k > 1.75$) or brittle ($k < 1.75$) behavior of a material. H_V is related to the hardness of the mineral during indentation (resistance to plastic deformations).

The interested reader can find applications of the algorithms and formulations here briefly presented in other works (Ulian et al. 2014, 2018; Ulian and Valdrè 2015c, 2017, 2018a, 2018b, 2018c, 2019a, 2019b).

Finally, the direct piezoelectric e and dielectric ε tensors were evaluated through a coupled perturbed Kohn-Sham (CPKS) approach, as recently implemented in the CRYSTAL code (Baima et al. 2016).

Lattice dynamics and thermodynamic properties

Harmonic phonon frequencies were calculated by diagonalization of the dynamical matrix using the direct space method, whose details are provided in specific literature (Parlinski et al. 1997; Wallace 1998; Togo and Tanaka 2015). We considered the effect of the longitudinal optical (LO) and transverse optical (TO) splitting in the phonon dispersion (Wang et al. 2010). The LO-TO splitting gives rise to a non-analytical contribution on the phonon bands and depends on the electronic (clamped nuclei) dielectric tensor ε_0 and on the Born effective charge tensor associated with each atom. We calculated both quantities through a coupled-perturbed Kohn-Sham (CPKS) approach (Pascale et al. 2004; Ferrero et al. 2008). Numerical convergence on the results was checked against three isotropic supercells with 32, 108, and 256 atoms (labeled as SC32, SC108, and SC256, respectively), leading to the sampling of 8, 27, and 64 **q** points in the reciprocal space, respectively. To increase the **q** point sampling and increase the quality of the thermodynamic results, we employed a Fourier interpolation method using an isotropic $4 \times 4 \times 4$ mesh (Dovesi et al. 2018), obtaining a total of 512, 1728, and 4096 **q** points for the SC32, SC108, and SC256 supercells, respectively.

Standard statistical thermodynamics on harmonic phonon frequencies cannot provide a good description of thermodynamic and mechanic data at different P-T conditions. Thus, we employed the quasi-harmonic approximation (QHA), which describes the phonon of the system as volume dependent and overcomes the issue related to the harmonic approximation (e.g., zero thermal expansion). Several methods within the QHA framework have been proposed and employed in literature (Ottonello et al. 2010; Prencipe et al. 2011; Erba 2014; Erba et al. 2015; Ulian and Valdrè 2015a, 2015b, 2015c, 2018d, 2019b; Belmonte et al. 2017), and here we adopted the one discussed by Belmonte (2017) for periclase. The interested reader can find complete details on this approach in QHA in the cited work, whereas, for the sake of completeness, some of the main steps involved in the calculations are reported in the Appendix[1].

Results and discussion

Equation of state

We reported in Table 1 the structural data on both the equilibrium geometry and the different unit cells of wurtzite under compression. The static energy vs. unit-cell volume curves, $E(V)$, are well fitted by the volume-integrated BM3 fit reported in Equation 1, which resulted in $K_0 = 72.17(4)$ GPa, $K' = 3.87(1)$, and $V_0 = 85.781(1)$ Å^3. The bulk modulus value is in good agreement with the very recent theoretical results of Valdez and coworkers (2019), who obtained $K_0 = 74.3$ GPa by employing planewaves basis set and the Perdew-Burke-Ernzerhof (Perdew et al. 1996) DFT functional. In the work of Sharma et al. (2019), simulations with DFT/PBE plus Hubbard correction (DFT+U) resulted in bulk modulus and its pressure derivative 81.9 GPa and 3.96, respectively, which are also close to ours. It can be noted the systematic increase in the K_0 values previously obtained, which is a common figure when the PBE functional is adopted, is related to the high repulsive core-valence exchange in generalized-gradient approximation (GGA).

Table 1. Wurtzite unit-cell volume, lattice parameters and bond distances and angles calculated at different hydrostatic compressions and in static conditions

P (GPa)	V (Å^3)	a (Å)	c (Å)	d1 (Å)	d2 (Å)	θ (°)
22.1	70.145	3.6620	6.0397	2.251	2.248	110.05
17.2	72.495	3.7072	6.0908	2.275	2.275	109.80
12.5	75.142	3.7550	6.1538	2.302	2.303	109.64
8.5	77.856	3.8020	6.2192	2.329	2.332	109.52
5.1	80.635	3.8485	6.2864	2.356	2.360	109.43
1.8	83.792	3.8997	6.3621	2.386	2.391	109.34
0.4	85.282	3.9233	6.3976	2.400	2.405	109.31
−0.5	86.400	3.9408	6.4240	2.411	2.416	109.29
−2.8	89.387	3.9867	6.4940	2.438	2.444	109.24
−4.7	92.441	4.0324	6.5645	2.465	2.472	109.20
−6.4	95.563	4.0780	6.6354	2.492	2.500	109.15

Notes: d1 and d2 are referred to Zn-S bonds, whereas θ is the S-Zn-S bond angle. Pressure values were obtained using the volume-integrated EoS parameters in the pressure-volume formulation of the third-order Birch-Murnaghan equation.

The zero-pressure unit-cell parameters (a = 3.9233 Å, c = 6.3976 Å) are in good agreement with the theoretical ones calculated at the Hartree-Fock (HF) limit by Catti et al. (2003) (a = 3.982 Å, c = 6.500 Å) and the results of Valdez and coworkers (2019) obtained with DFT/PBE approach (a = 3.89 Å, c = 6.38 Å). It is worth noting that the pressure state of the equilibrium geometry is less than 10^{-5} GPa (10^{-1} atm), as observed from the forces acting on the unit cell after geometry optimization. The value reported in Table 1 was calculated from Equation 2 using the BM3 parameters previously described.

Regarding the internal geometry of the mineral, there is an inverse relationship between pressure and the length of the non-equivalent Zn-S bonds (the minor labeled as d1 and the major as d2 in Table 1), whereas there is a direct proportionality with the S-Zn-S angle.

Electronic band structure

We reported the band gaps calculated at the B3LYP level at 0 K in Table 2. Band structure along the path Γ-A-L-M-Γ-A-H-K-A in the First Brillouin zone together with the total and orbital-projected density of states (DOSS) are presented graphically in Figure 2. At equilibrium (Fig. 2a), the gap between the valence and conductive bands is of the direct type, with $E_g = 4.87$ eV, and the increase of the hydrostatic pressure widens the bandgap with a nonlinear trend. At about 17 GPa and above (Fig. 2b), the bandgap becomes an indirect one, which is an electronic feature of the rock-salt (high-pressure) ZnS polymorph (Cardona et al. 2010; Ulian and Valdrè 2019b). A similar result was obtained in previous simulations at the DFT/PW level of theory by Hu et al. (2008). The top of the valence band is dominated by the 3p states of sulfur, whereas the bottom of the conduction band is given mainly by 4s states of zinc.

Let us discuss these results with those in literature obtained with different approaches. The experimental value of the bandgap of wurtzite is 3.87 eV (Madelung and Schulz 1982). In this sense, the present result is overestimated by about 1 eV, which is not surprising due to the chosen Hamiltonian. The formulation of the hybrid functional B3LYP contains 20% of Hartree-Fock

contribution to the total energy. Pure HF is known to highly overestimate the bandgap of solids, but this effect is reduced by the GGA contribution that underestimates the same property. Indeed, recent calculations with pure GGA-PBE approach showed E_g values well below 2.5 eV (Karazhanov et al. 2006; Sharma et al. 2019; Valdez et al. 2019), and the addition of the Hubbard correction allowed obtaining results in better agreement with experiments ($E_g \approx 3.87$ eV). Previous simulations with a semi-ab initio approach known as orthogonalized linear combination of atomic orbitals (OLCAO), based on the Kohn-Sham form of the exchange-correlation potential, resulted in a direct bandgap of about 3.3 eV (Xu and Ching 1993). Notwithstanding the different E_g values obtained with each approach, we obtained band structure features that are in good agreement with all previous simulations.

TABLE 2. Calculated band gap (E_g, eV) and band gap type of wurtzite at different compression states

P (GPa)	E_g (eV)	Type
22.1	5.652	indirect
17.2	5.641	indirect
12.5	5.508	direct
8.5	5.372	direct
5.1	5.174	direct
1.8	4.957	direct
0.4	4.862	direct
–0.5	4.788	direct
–2.8	4.600	direct
–4.7	4.415	direct
–6.4	4.235	direct

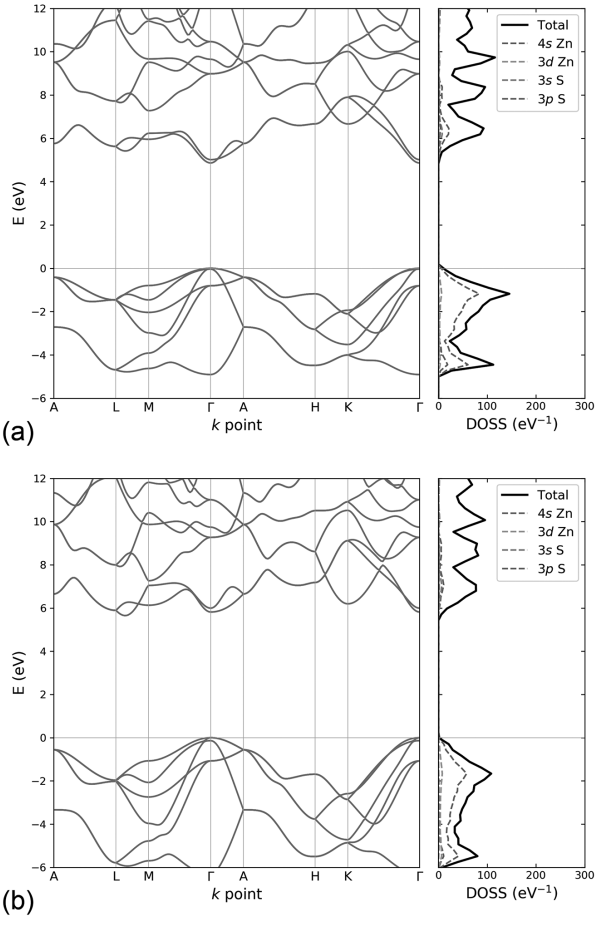

FIGURE 2. Electronic band structure and density of states of wurtzite (**a**) at equilibrium and (**b**) at P = 22 GPa, both at 0 K.

Elastic properties

As explained in the methods section, we calculated the second-order elastic moduli of wurtzite at each unit-cell volume, including a correction for the pressure state of the system. For the sake of brevity, we reported in Table 3 only the results obtained at equilibrium. The complete results (elastic constants, piezoelectric constants, dielectric tensor, and density), together with derived data (bulk, shear ad Young's moduli, Poisson's and Pugh ratio, Vickers hardness) are reported in Supplemental[1] Table S1.

It is possible to evaluate the mechanical stability of minerals from the values of the elastic moduli. For wurtzite, which has an hexagonal unit cell, the well-known Born stability criteria are given by the following three relations: (1) $\tilde{C}_{44} > 0$, (2) $\tilde{C}_{11} > |\tilde{C}_{12}|$, and (3) $2\tilde{C}_{13}^2 - \tilde{C}_{33}(\tilde{C}_{11} + \tilde{C}_{12}) < 0$, with $\tilde{C}_{\alpha\alpha} = C_{\alpha\alpha} - P$ for $\alpha = 1, 4$, and $\tilde{C}_{1\alpha} = C_{1\alpha} + P$ (Born and Huang 1954). As can be observed from Figure 3, the stability criteria 1 and 2 are not satisfied when the pressure is above 19.1 and 20.5 GPa, respectively. In addition, the trend of curve $C_{44}(P)$ also shows an elastic softening with pressure. The third criterion, not shown in Figure 3, is respected in the investigated pressure range. This analysis shows that upon compression, the wurtzite phase is not stable above about 19 GPa at the static (0 K) limit, which is in agreement with previous simulations at the local-density approximation (LDA) level of theory (Ferahtia et al. 2014).

The elastic properties obtained with the DFT/B3LYP approach at equilibrium are in good agreement with previous theoretical results. With respect to Hartree-Fock (HF), we obtained higher values of the elastic moduli, whereas those calculated at generalized-gradient approximation level of theory (PBE functional) are generally lower, with the exception of the C_{12} modulus (Catti et al. 2003; Valdez et al. 2019). This is a common figure in DFT simulations, where standard GGA approaches result in smaller unit-cell volume and higher bulk modulus (and consequently, elastic constants).

In comparison with experimental data, the present results

TABLE 3. Second-order elastic constants (reported in GPa), piezoelectric constants (C m^{-2}) and polycrystalline averages of wurtzite at equilibrium geometry

	B3LYP[a]	PBE[b]	LDA[c]	HF[d]	Exp[e]	Exp[f]	Exp[g]
C_{11}	119.1	125.7	135.46	118	124	122	
C_{12}	55.8	52.86	65.89	52	60	59	
C_{13}	44.4	47.5	51.63	39	45	46	
C_{33}	136.7	135.2	160.77	135	140	138	
C_{44}	28.1	33.6	29.73	31	29	28	
e_{33}	0.25		0.161	0.18			0.34
e_{31}	–0.16		–0.160	–0.13			–0.10
e_{15}	–0.12		–0.105	–0.13			–0.08
K	73.5	75.8	85.52	70.1	76.4	76.0	
μ	32.6	36.5	35.57	34.6	33.3	32.4	
E	85.3	94.3	93.71	89.2	87.3	85.1	
υ	0.31	0.29	0.32	0.29	0.31	0.31	
k	0.44	0.49	0.42	0.48	0.44	0.43	
H_v	2.9	4.0	2.8	4.0	2.9	2.6	

Notes: K, μ, E, υ, and are the polycrystalline averages of the bulk modulus (GPa), shear modulus (GPa), Young's modulus (GPa), and Poisson's ratio, respectively. k is the Pugh ratio μ/K and H_v is the Vickers hardness (GPa). [a] Present work; [b] Valdez et al. (2019); [c] Ferahtia et al. (2014); [d] Catti et al. (2003); [e] Cline et al. (1967); [f] Uchida and Saito (1972); [g] Landolt-Börnstein (1986).

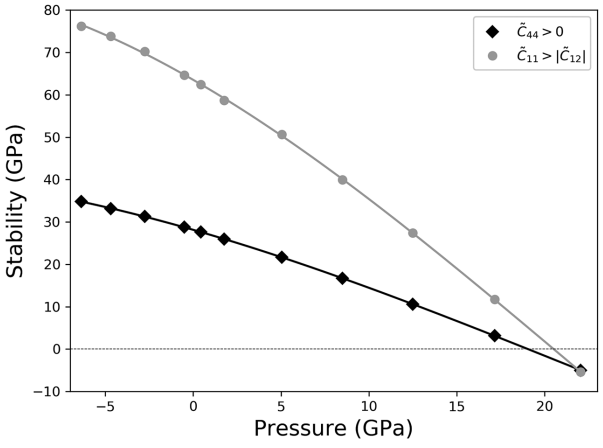

Figure 3. Graphical representation of the mechanical stability criteria $\tilde{C}_{44} > 0$ and $\tilde{C}_{11} > |\tilde{C}_{12}|$ of wurtzite under pressure.

are in excellent agreement, even if they were obtained at 0 K and without the inclusion of zero-point vibrational contributions (Cline et al. 1967; Uchida and Saito 1972). The mean standard deviation on the calculated values is 2.9, which is lower respect the results of Catti et al. (2003), Ferahtia et al. (2014), and Valdez et al. (2019), calculated at the HF, LDA, and generalized-gradient approximation with PBE functional, respectively.

Single-crystal mechanical properties calculated in different crystallographic directions are reported in Figure 4, together with previous theoretical and experimental results. For the sake of an example, in Figure 4a, it is possible to observe that the maxima of the Young's modulus in wurtzite calculated on the $(10\bar{1}0)$ plane reside in the principal crystallographic directions, whereas the minima were calculated at 45° respect to **c**-axis direction. In addition, this phase shows an isotropic behavior in the (0001) plane (not shown in the figure).

As previously mentioned, we calculated and reported in Supplemental[1] Table S1 the bulk (K) and shear (μ), moduli for

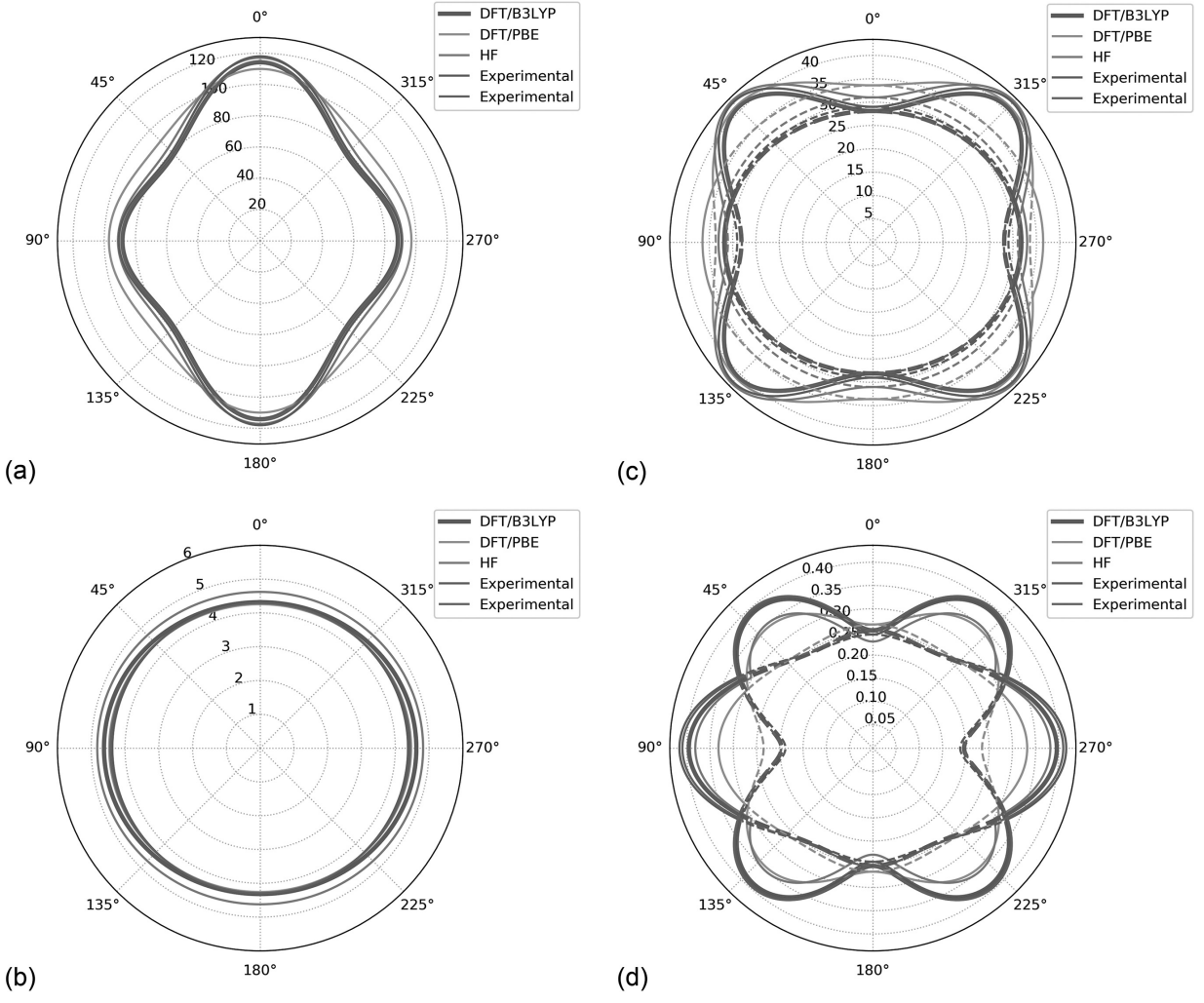

Figure 4. (**a**) Young's modulus (GPa), (**b**) linear compressibility ($1/K$, GPa^{-1}), (**c**) shear modulus (GPa) and (**d**) Poisson's ratio for the $(10\bar{1}0)$ plane of wurtzite. DFT/PBE (Valdez et al. 2019) and Hartree-Fock (Catti et al. 2003), together with the experimental results of Cline and coworkers (1967) (red line) and of Uchida and Saito (1972) (purple line) are reported for a graphical comparison. In **c** and **d**, the continuous lines are related to the maximum values, whereas the dashed ones to the minimum values.

monocrystals, according to the formulation of Nye (1957). In Table 3, we reported only the results from the Voigt-Reuss-Hill (VRH) averages for polycrystalline aggregates (Hill 1952), which includes Young's (E) modulus and Poisson's ratio.

The calculated Pugh's ratio and Vicker's hardness, k and H_V, respectively, are in good agreement with all previous experimental and theoretical results (Cline et al. 1967; Uchida and Saito 1972; Catti et al. 2003; Chen et al. 2011; Ferahtia et al. 2014; Valdez et al. 2019). It is interesting to note that the hardness and the k ratio of wurtzite decreases as pressure is raised, which means that the mineral becomes more ductile as pressure augments. In addition, the H_V value becomes negative at the maximum explored pressure, which is in agreement with the failure of the stability criteria previously discussed (see Supplemental[1] Table S1).

Regarding the piezoelectric constants, hexagonal crystals possess three independent tensor components, e_{33}, e_{31}, and e_{15}. The values calculated at the B3LYP level are in good agreement with both the experimental (Landolt-Börnstein 1986) and previous theoretical data reported in the literature (Catti et al. 2003; Ferahtia et al. 2014). The slightly larger discrepancy on the experimental e_{33} piezoelectric constant is due to the presence of defects in the real crystal sample of wurtzite used in the tests, as also pointed out by Catti et al. (2003).

Phonon properties

In the first step for the evaluation of the lattice dynamics of wurtzite, we calculated the Γ-point (**k** = 0) vibrational modes of the system, which were reported in Table 4. In details, the irreducible representation of the normal modes of wz-ZnS is the following:

$$\Gamma_{tot} = 2A + 2B + 2E_1 + 2E_2$$

with the first $A + E_1$ modes being acoustic. A and E_1 vibrational modes are active in both Raman and infrared spectroscopies and are subject to the LO-TO splitting. E_2 modes are Raman-active and B modes are silent.

It is interesting to note that the vibrational frequency of each mode increases with pressure, meaning positive isotropic mode-Grüneisen parameters $\gamma_i = -(\partial \ln \nu_i / \partial \ln V)$, with the subscript i indicating the i-th vibrational mode. The only exception is the lowest E_2 normal mode, whose γ_i value is negative, showing that the frequency decreases by increasing pressure (decreasing unit-cell volume). Considering the low frequency of this vibrational mode, this result suggests a possible phonon softening (negative frequency value) at higher pressure, which could be related to a phase transition from wurtzite to the rock-salt structure. Differently from elastic and thermodynamic analyses, it is not straightforward to establish the exact transition pressure from the ab initio trends of the $\nu(V)$ curves. However, they can represent a stability indicator, as we recently showed with the rock-salt phase of ZnS, which is phononically unstable at low pressures (Ulian and Valdrè 2019b).

The LO-TO splitting is quite remarkable for the modes interested in this phenomenon, with differences between the transverse optical-longitudinal optical frequencies (marked with Δ in Table 4) up to about 100 cm^{-1}.

Born charges evaluated at Γ-point for the equilibrium geometry of wurtzite are in agreement with the expected values for a zinc sulfide; namely we obtained +2.06 and –2.06 for zinc and sulfur, respectively, in good agreement with the ±1.89 reported by Kang et al. (2017). The charges vary slightly by applying pressure to the system, with values of ±1.85 at 22.05 GPa and ±2.18 at –6.37 GPa.

As mentioned in the Methods section, to calculate reliable thermodynamic quantities, we calculated the phonon dispersion relations using a direct space approach on supercells of increasing size. A graphical representation of the phonon bands and phonon density of states (DOS) is reported in Figure 5 at equilibrium geometry (Fig. 5a) and at the maximum explored pressure (Fig. 5b). In the M → Γ phonon branch, it can be noted a very small inflection of an acoustic phonon, which is the result of some numerical noise related to the interpolation of the data during the construction of the phonon dispersion bands. The phonon DOS clearly shows that at low frequency the bands are dominated by zinc vibrations, whereas at higher wavenumbers sulfur plays the major role. The calculated phonon dispersion relations and the phonon density of states are in good agreement with the previous experimental and theoretical results reported in the literature (Hu et al. 2008; Bachmann et al. 2012).

In addition, we found a very good phonon continuity over the explored unit-cell volumes (pressure), which means that the variations of the phonon frequency values as a function of the volume are monotonic. Indeed, a third-order polynomial fit on each phonon band resulted in a mean R^2 of 9.991×10^{-1}. This

TABLE 4. Γ-point frequencies (cm^{-1}) of wurtzite-2*H* at different pressures, calculated at the DFT/B3LYP level of theory taking into account the LO-TO splitting

Modes		Pressure (GPa)											DFT[a]	Exp[b]
		22.1	17.2	12.5	8.5	5.1	1.8	0.4	−0.5	−2.8	−4.7	−6.4		
E_2	(TO)	47.7	57.1	64.2	69.8	73.9	77.5	78.9	79.7	81.5	82.5	83.3	72.9	72.5
B	(TO)	239.3	232.6	226.4	220.5	214.7	207.6	204.6	202.3	196.2	190.0	183.6	193.8	–
A	(TO)	366.6	346.7	327.3	308.6	291.2	272.8	264.5	258.3	242.7	227.8	213.2	277.6	273.3
	(LO)	435.2	419.1	403.5	388.9	375.4	361.1	354.8	350.1	338.3	327.2	316.5	332.9	351.1
	Δ	68.6	72.4	76.3	80.3	84.2	88.4	90.3	91.8	95.6	99.4	103.3		
E_1	(TO)	362.1	346.3	329.1	312.0	295.7	278.7	270.9	265.0	250.2	235.7	221.8	277.6	273.3
	(LO)	427.5	414.7	401.1	387.4	374.6	361.5	355.7	351.1	339.8	329.0	318.6	337.3	351.1
	Δ	65.4	68.4	71.9	75.4	78.9	82.8	84.7	86.1	89.7	93.3	96.8		
E_2	(TO)	376.3	359.1	340.1	321.6	303.8	285.1	276.6	270.4	254.2	238.3	223.4	283.4	286.0
B	(TO)	422.2	404.4	386.5	370.3	354.6	338.6	331.5	326.3	313.7	302.2	291.7	283.4	286.0

Notes: Δ is the difference between the longitudinal and transversal optical frequency.
[a] Kang et al. (2017).
[b] Brafman and Mitra (1968).

observation is important for the subsequent calculations of the mineral thermodynamics (*vide infra*).

Thermodynamic and thermoelastic properties

By combining the static equation of state and the phonon frequency dependence on volume (pressure), we are able to calculate several thermodynamic and thermoelastic data on wurtzite via the quasi-harmonic approximation (see Computational Methods section for details). We considered for this scope a pressure range of 0–20 GPa and temperatures between 0 and 2000 K. It is worth noting that 0 K data obtained by means of the QHA approach are not the same as in static calculations, because here the zero-point thermal contribution is included in the treatment.

In Table 5, we present thermodynamic and elastic data of wurtzite calculated at 300 K as a function of pressure. Conversely, we report in Figure 6 some selected properties of interest, calculated at zero-pressure conditions, where it is possible to observe that the results are numerical converged when calculated on a supercell with 108 atoms. More into details, thermodynamic quantities are converged within 0.6%, whereas elastic properties (e.g., isothermal bulk modulus, K_T) within 1.2%. Albeit increasing the **k** sampling did not significantly increase the accuracy of the QHA approach, the following discussion and results will be focused on the results from SC256 (256 atoms in the supercell).

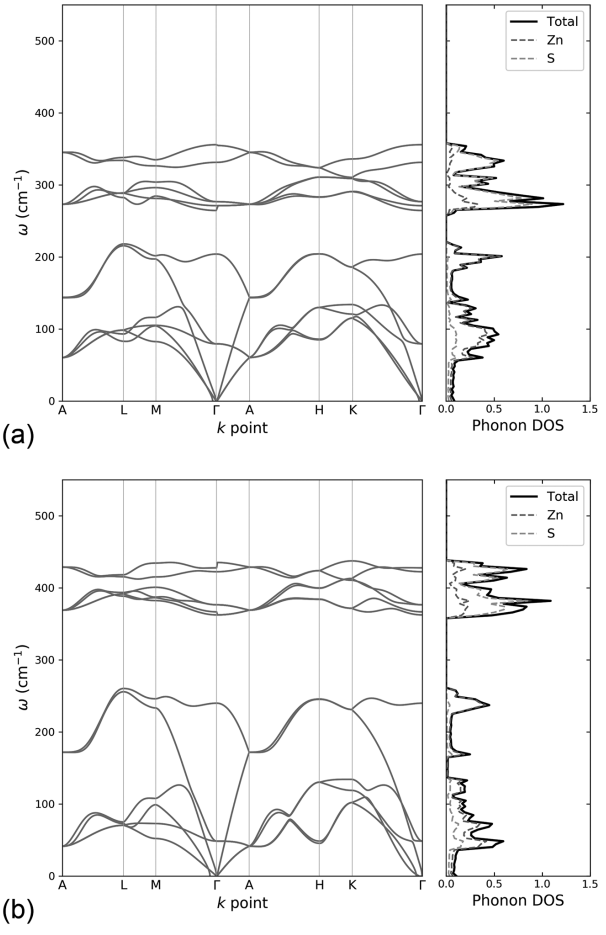

Figure 5. Phonon dispersion and phonon density of states (DOS) of wurtzite ZnS calculated (**a**) at equilibrium geometry and (**b**) at 22.05 GPa.

The calculated thermodynamics is in very good agreement with previous low- and high-temperature calorimetric measurements (Pankratz and King 1965; Stuve 1974; Robie and Hemingway 1995). For example, the standard state entropy calculated by the present ab initio approach is 58.49 J/(mol·K), which is very close to the measured value of 58.83 ± 0.17 J/(mol·K) (–0.6%). Also, the theoretical thermal evolution of both entropy (Fig. 6a), heat capacity (Fig. 6b) and enthalpy (as $H_T - H_{300}$, Fig. 6c) fall between about 1–2% of the experimental values, a result consistent with the previous theoretical prediction of these properties by ab initio methods (Belmonte et al. 2016).

Regarding the volumetric thermal expansion coefficient, it can be noted from Figure 6d that at very low temperatures the $\alpha_V(T)$ values are slightly negative, which is due not surprisingly to the E_2 phonon bands with negative Grüneisen parameter, as also reported by Biernacki and Scheffler (1989). At 300 K and 0 GPa, the calculated thermal expansion coefficient is 2.16×10^{-5}, which is in line with previous experimental and theoretical findings with α_V (300 K) between 1.62×10^{-5} and 2.57×10^{-5} (Majumdar and Roy 1965; Wang 2006; Valdez et al. 2019).

We reported in Figure 6e the isothermal and adiabatic bulk moduli of wurtzite calculated at zero pressure as a function of temperature, which shows the expected thermal trend. From the elastic properties point of view, these values represent the Reuss lower bound that can be calculated from the elastic moduli at different temperature and pressure states. At 300 K, we obtained $K_T = 68.6(6)$ GPa, $K'_T = 4.01(13)$, and $K_S = 68.9$ GPa, with an isothermal bulk modulus that is slightly lower than those reported by Desgreniers et al. (2000) and by Chang and Barsch (1973), whose values were 80.1 and 75.8 GPa, respectively.

We report in Figure 7, for the sake of completeness, some selected thermodynamic and thermoelastic properties of wurtzite as a function of both temperature and pressure, which could be

Table 5. DFT/B3LYP wz-ZnS molar volume, coefficient of thermal expansion (α_V), isothermal bulk modulus (K_T), and its pressure derivative (K'_T), adiabatic bulk modulus (K_S), entropy (S), and isobaric heat capacity (C_P) in the pressure range 0–20 GPa and at 300 K

P (GPa)	V (Å^3 mol^{-1})	α_V (10^{-6} K^{-1})	K_T (GPa)	K'_T	K_S (GPa)	S [J/(mol·K)]	C_P [J/(mol·K)]
0	43.22(2)	21.635	68.6(6)	4.01(13)	68.9	58.49	45.46
1	42.61(2)	18.777	72.6(5)	4.00(12)	72.8	57.98	45.25
2	42.04(2)	16.592	76.5(4)	3.95(12)	76.8	57.51	45.06
3	41.51(2)	16.299	80.5(3)	3.91(12)	80.8	57.10	44.92
4	41.01(2)	14.341	84.4(3)	3.86(12)	84.6	56.73	44.74
5	40.54(3)	13.230	88.(3)	3.82(12)	88.5	56.40	44.59
6	40.09(2)	11.440	92.1(3)	3.78(12)	92.2	56.11	44.42
7	39.67(3)	10.333	95.8(4)	3.73(12)	96.0	55.84	44.27
8	39.26(2)	9.226	99.6(5)	3.69(12)	99.7	55.61	44.13
9	38.88(2)	8.525	103.2(6)	3.65(12)	103.4	55.40	43.99
10	38.51(2)	7.702	106.9(7)	3.61(12)	107.0	55.21	43.85
11	38.16(2)	6.771	110.5(8)	3.57(12)	110.5	55.05	43.72
12	37.82(2)	6.142	114.0(9)	3.52(12)	114.1	54.90	43.59
13	37.49(2)	5.724	118(1)	3.49(12)	117.6	54.78	43.46
14	37.18(2)	4.250	121(1)	3.44(12)	120.9	54.66	43.33
15	36.88(3)	3.983	124(1)	3.40(12)	124.3	54.57	43.21
16	36.59(3)	4.187	128(1)	3.36(13)	127.7	54.48	43.09
17	36.30(4)	3.471	131(2)	3.32(12)	131.0	54.41	42.97
18	36.03(4)	1.520	134(2)	3.28(13)	134.2	54.36	42.85
19	35.77(5)	-0.245	137(2)	3.24(13)	137.3	54.31	42.73
20	35.51(6)	1.352	140(2)	3.20(13)	140.4	54.27	42.62

Note: In parentheses, the standard deviations calculated by the volume-integrated third-order Birch-Murnaghan equation of state are reported.

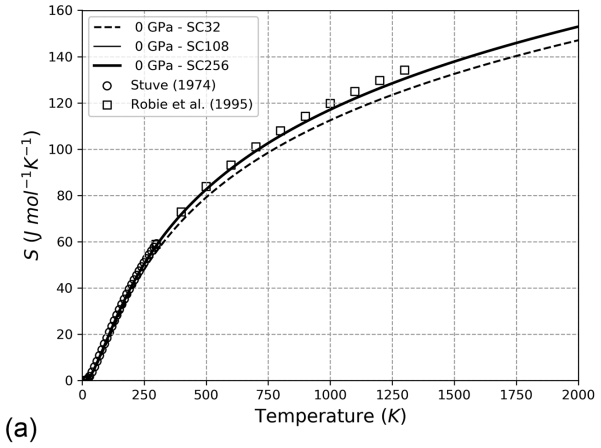

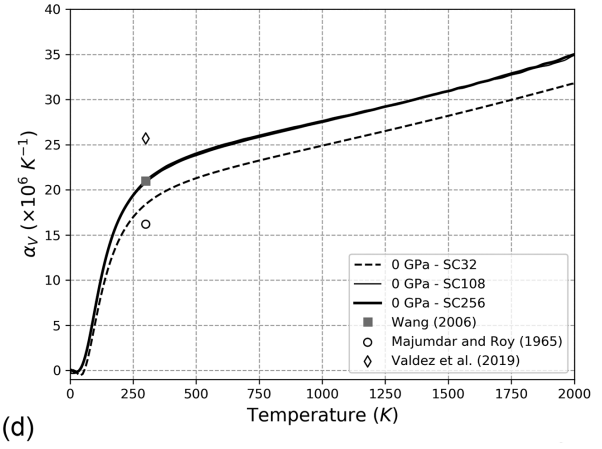

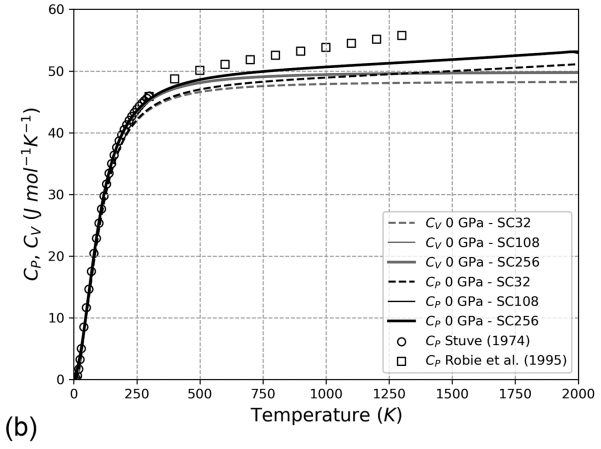

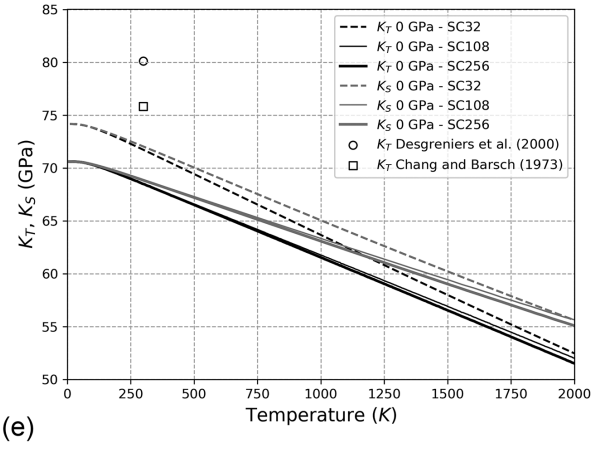

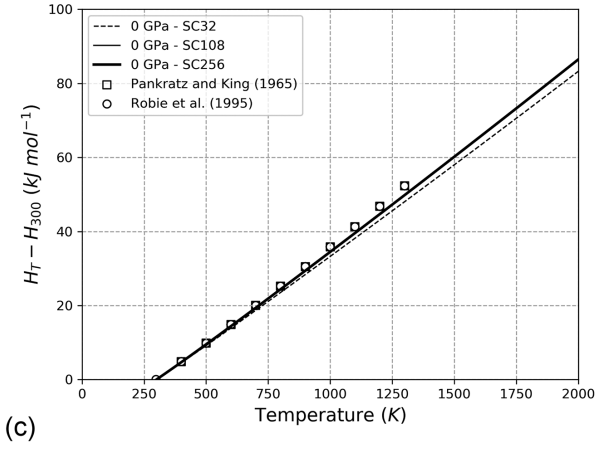

Figure 6. Selected thermodynamic and elastic properties of wurtzite at 0 GPa between 0 and 2000 K, calculated on supercells (SC) of increasing size (32, 108, and 256 atoms in SC32, SC108, and SC265, respectively). (**a**) Entropy, (**b**) isochoric, C_V, and isobaric, C_P, heat capacities, (**c**) enthalpy (as H_T–H_{300}), (**d**) volumetric thermal expansion coefficient, α_V, and (**e**) isothermal, K_T, and adiabatic, K_S, bulk moduli (corresponding to the Reuss lower bound).

useful for data extraction and comparison with future works.

Finally, we report in Figure 8, the zero-pressure relative volume variation with pressure at 300 K, in comparison with the experimental data of Desgreniers et al. (2000). It is possible to observe an excellent agreement between our DFT/B3LYP results and the experimental ones between 0 and 5 GPa, then there is a small deviation (about 3% at 20 GPa), resulting in a softer behavior of wurtzite as a function of pressure. This discrepancy could be due to several reasons. The first one is that we simulated an ideal single-crystal of wurtzite, whereas the sample experimentally investigated was ground to a fine powder prior to the analysis in the diamond-anvil cell. Second, the authors reported a partial wurtzite → zinc-blende transformation during the grinding procedure, thus the powders contained a mixture of the two phases. Finally, when the wurtzite sample was compressed, it transformed into the zinc-blende structure prior to a transition at higher pressure to the rock-salt structure, and these two phases coexisted between from 12.4 to 13.5 GPa. These observations could also explain the discrepancy reported on the calculated bulk modulus.

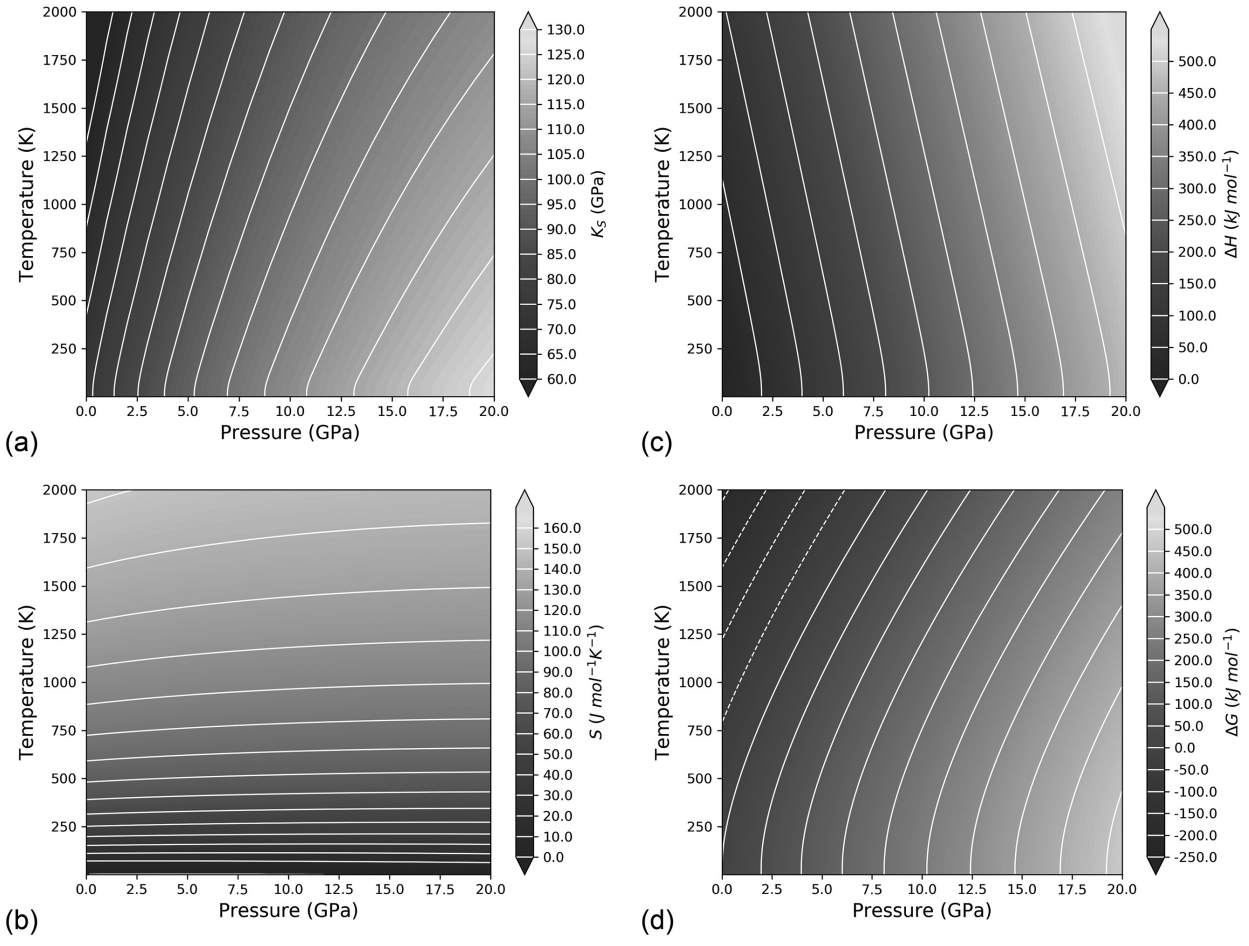

Figure 7. Contour maps in the pressure and temperature ranges 0–20 GPa and 0–2000 K, respectively, of (**a**) adiabatic bulk modulus (Reuss lower bound), (**b**) entropy, (**c**) enthalpy, and (**d**) Gibbs free energy. (**c** and **d**) The reported difference is related to the wurtzite at zero pressure and temperature.

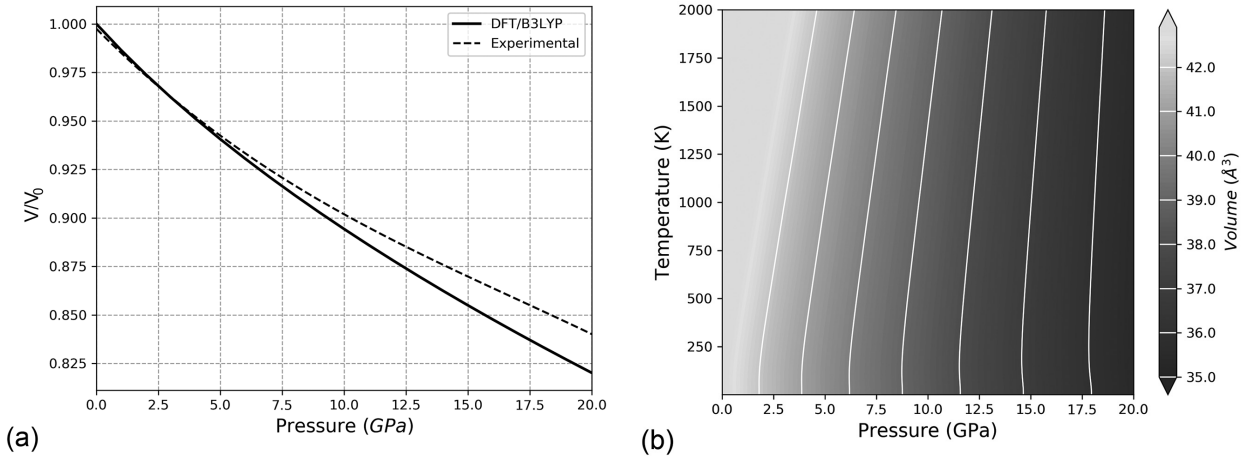

Figure 8. (**a**) Relative unit cell of wurtzite at 300 K as a function of pressure, calculated at the DFT/B3LYP level of theory, compared to the experimental results of Desgreniers et al. (2000). (**b**) Contour maps of the wurtzite unit cell in the pressure and temperature ranges 0–20 GPa and 0–2000 K, respectively.

Implications

Because wurtzite an important mineral phase in scientific and technological fields spanning from geology/mineralogy to material science, the present work provided deep insights on its thermodynamic, thermomechanical, and electronic properties that can be useful for various applications. To cite some examples, the thermoelastic behavior of wz-ZnS showed that this mineral is unstable at high pressure, and, considering also previous experimental and theoretical works, it should transform to the rock-salt ZnS structure below the Earth's surface. The piezoelectric and elastic constants, electronic band structure, and density of states are very important for industrial applications of wurtzite, because they could help to design a semiconductor material with tailored properties or, linked to the previous geological consideration, develop pressure sensors based on the direct-indirect bandgap.

Wurtzite is also a model system for diamond-like structures presenting ionic bonds and many important minerals and semiconductors are isostructural with wz-ZnS, hence detailed elastic and thermodynamic data are useful to compare the effects of cationic/anionic substitutions and other crystal-chemical variations.

As a final note, the theoretical approach here employed, based on a combination of static (0 K) and thermal (QHA) methods, proved to be consistent and sound. The hybrid density functional theory functionals (as B3LYP) are also a very good choice for the prediction of thermodynamic properties of different kinds of minerals and compounds. This is important to obtain fundamental data at pressure and temperature conditions that are still difficult and expensive to be obtained experimentally. Indeed, a proper calibration of the static/QHA approach is a powerful predicting tool able to provide detailed analyses of phases of interest for different and manifold fields of applications.

References cited

Adachi, S. (2005) Properties of Group IV, III-V, and II-VI Semiconductors. Wiley.

Bachmann, M., Czerner, M., Edalati-Boostan, S., and Heiliger, C. (2012) Ab initio calculations of phonon transport in ZnO and ZnS. European Physical Journal B, 85(5), 146.

Baima, J., Erba, A., Maschio, L., Zicovich-Wilson, C.M., Dovesi, R., and Kirtman, B. (2016) Direct piezoelectric tensor of 3D periodic systems through a coupled perturbed Hartree-Fock/Kohn-Sham method. Zeitschrift für Physikalische Chemie-International Journal of Research in Physical Chemistry & Chemical Physics, 230(5-7), 719–736.

Barron, T.H.K., and Klein, M.L. (1965) Second-order elastic constants of a solid under stress. Proceedings of the Physical Society, 85, 523–532.

Becke, A.D. (1993a) Density-functional thermochemistry. III. The role of exact exchange. Journal of Chemical Physics, 98(7), 5648–5652.

——— (1993b) A new mixing of Hartree-Fock and local Density-Functional Theories. Journal of Chemical Physics, 98(2), 1372–1377.

Bellefleur, G., Schetselaar, E., White, D., Miah, K., and Dueck, P. (2015) 3D seismic imaging of the Lalor volcanogenic massive sulphide deposit, Manitoba, Canada. Geophysical Prospecting, 63(4), 813–832.

Belmonte, D. (2017) First principles thermodynamics of minerals at HP-HT conditions: MgO as a prototypical material. Minerals 7, 183.

Belmonte, D., Gatti, C., Ottonello, G., Richet, P., and Zuccolini, M.V. (2016) Ab initio thermodynamic and thermophysical properties of sodium metasilicate, Na_2SiO_3, and their electron-density and electron-pair-density counterparts. Journal of Physical Chemistry A, 120(44), 8881–8895.

Belmonte, D., Ottonello, G., Zuccolini, M.V., and Attene, M. (2017) The system MgO-Al_2O_3-SiO_2 under pressure: A computational study of melting relations and phase diagrams. Chemical Geology, 461, 54–64.

Biernacki, S., and Scheffler, M. (1989) Negative Thermal-Expansion of Diamond and Zincblende Semiconductors. Physical Review Letters, 63(3), 290–293.

Birch, F. (1947) Finite elastic strain of cubic crystal. Physical Review, 71, 809–824.

Born, M., and Huang, K. (1954) Dynamical Theory of Crystal Lattices. Clarendon Press, Oxford.

Brafman, O., and Mitra, S.S. (1968) Raman effect in wurtzite- and zinc-blende-type ZnS single crystals. Physical Review, 171, 931.

Brainerd, J.G. (1949) Standards on piezoelectric crystals. Proceedings of the IRE, 37, 1378–1395.

Cardona, M., Kremer, R.K., Lauck, R., Siegle, G., Munoz, A., Romero, A.H., and Schindler, A. (2010) Electronic, vibrational, and thermodynamic properties of ZnS with zinc-blende and rocksalt structure. Physical Review B, 81(7).

Catti, M., Noel, Y., and Dovesi, R. (2003) Full piezoelectric tensors of wurtzite and zinc blende ZnO and ZnS by first-principles calculations. Journal of Physics and Chemistry of Solids, 64(11), 2183–2190.

Chang, E., and Barsch, G.R. (1973) Pressure dependence of single crystal elastic constants and anharmonic properties of wurtzite. Journal of Physics and Chemistry of Solids, 34(9), 1543–1563.

Chen, X.Q., Niu, H., Li, D., and Li, Y. (2011) Modeling hardness of polycrystalline materials and bulk metallic glasses. Intermetallics, 19(9), 1275–1281.

Cline, C.F., Dunegan, H.L., and Henderson, G.W. (1967) Elastic constants of hexagonal BeO, ZnS, and CdSe. Journal of Applied Physics, 38, 1944–1948.

Desgreniers, S., Beaulieu, L., and Lepage, I. (2000) Pressure-induced structural changes in ZnS. Physical Review B, 61(13), 8726–8733.

Doll, K. (2001) Implementation of analytical Hartree-Fock gradients for periodic systems. Computer Physics Communications, 137, 74–78.

Doll, K., Harrison, N.M., and Saunders, V.R. (2001) Analytical Hartree-Fock gradients for periodic systems. Journal of Quantum Chemistry, 82(1), 1–13.

Dovesi, R., Erba, A., Orlando, R., Zicovich-Wilson, C.M., Civalleri, B., Maschio, L., Rerat, M., Casassa, S., Baima, J., Salustro, S., and Kirtman, B. (2018) Quantum-mechanical condensed matter simulations with CRYSTAL. Wiley Interdisciplinary Reviews-Computational Molecular Science, 8(4), E1360.

Erba, A. (2014) On combining temperature and pressure effects on structural properties of crystals with standard ab initio techniques. Journal of Chemical Physics, 141(12), 124115.

Erba, A., Mahmoud, A., Belmonte, D., and Dovesi, R. (2014) High pressure elastic properties of minerals from ab initio simulations: The case of pyrope, grossular and andradite silicate garnets. Journal of Chemical Physics, 140(12).

Erba, A., Maul, J., Demichelis, R., and Dovesi, R. (2015) Assessing thermochemical properties of materials through ab initio quantum-mechanical methods: the case of alpha-Al_2O_3. Physical Chemistry Chemical Physics, 17(17), 11670–11677.

Ferahtia, S., Saib, S., Bouarissa, N., and Benyettou, S. (2014) Structural parameters, elastic properties and piezoelectric constants of wurtzite ZnS and ZnSe under pressure. Superlattices and Microstructures, 67, 88–96.

Ferrero, M., Rerat, M., Orlando, R., and Dovesi, R. (2008) Coupled perturbed Hartree-Fock for periodic systems: The role of symmetry and related computational aspects. Journal of Chemical Physics, 128(1).

Frey, F., Jagodzinski, H., and Steger, G. (1986) On the phase-transformation zinc blends to wurtzite. Bulletin De Mineralogie, 109(1-2), 117–129.

Hebbache, M., and Zemzemi, M. (2004) Ab initio study of high-pressure behavior of a low compressibility metal and a hard material: Osmium and diamond. Physical Review B, 70(22).

Hill, R. (1952) The elastic behaviour of a crystalline aggregate. Proceedings of the Physical Society, London, Section A, 65, 349–354.

Hu, C.E., Zeng, Z.Y., Cheng, Y., Chen, X.R., and Cai, L.C. (2008) First-principles calculations for electronic, optical and thermodynamic properties of ZnS. Chinese Physics B, 17(10), 3867–3874.

Kandpal, K., and Gupta, N. (2018) Perspective of zinc oxide based thin film transistors: A comprehensive review. Microelectronics International, 35(1), 52–63.

Kang, Y.S., Zhao, G.J., and Liang, X.X. (2017) First-principle study of the lattice dynamic and thermodynamic properties of Zn-based semiconductors with wurtzite structure. Physica B-Condensed Matter, 515, 51–55.

Karazhanov, S.Z., Ravindran, P., Kjekhus, A., Fjellvag, H., Grossner, U., and Svensson, B.G. (2006) Electronic structure and band parameters for ZnX (X = O, S, Se, Te). Journal of Crystal Growth, 287(1), 162–168.

Kowalczuk, P.B., Snook, B., Kleiv, R.A., and Aasly, K. (2018) Efficient extraction of copper and zinc from seafloor massive sulphide rock samples from the Loki's Castle area at the Arctic Mid-Ocean Ridge. Minerals Engineering, 115, 106–116.

Landolt-Börnstein (1986) Landolt-Börnstein Tables. Springer.

Lee, C.T., Yang, W.T., and Parr, R.G. (1988) Development of the Colle-Salvetti Correlation-Energy formula into a functional of the electron-density. Physical Review B, 37(2), 785–789.

Madelung, O., and Schulz, M. (1982) Numerical Data and Functional Relationships in Science and Technology. New Series. Group III: Crystal and Solid State Physics. Springer, Berlin.

Majumdar, A.J., and Roy, R. (1965) Thermal expansion of ZnS from 2 to 317 K. Journal of Applied Physics, 38, 1531–1534.

Malehmir, A., Durrheim, R., Bellefleur, G., Urosevic, M., Juhlin, C., White, D.J., Milkereit, B., and Campbell, G. (2012) Seismic methods in mineral exploration and mine planning: A general overview of past and present case histories and a look into the future. Geophysics, 77(5), Wc173–Wc190.

Marmier, A., Lethbridge, Z.A.D., Walton, R.I., Smith, C.W., Parker, S.C., and Evans, K.E. (2010) ElAM: A computer program for the analysis and represen-

tation of anisotropic elastic properties. Computer Physics Communications, 181(12), 2102–2115.
Monkhorst, H.J., and Pack, J.D. (1976) Special points for Brillouin-zone integrations. Physical Review B, 8, 5188–5192.
Nye, J.F. (1957) Physical Properties of Crystals. Oxford University Press.
Ono, S., and Kikegawa, T. (2018) Phase transition of ZnS at high pressures and temperatures. Phase Transitions, 91(1), 9–14.
Ossai, C.I., and Raghavan, N. (2018) Nanostructure and nanomaterial characterization, growth mechanisms, and applications. Nanotechnology Reviews, 7(2), 209–231.
Ottonello, G., Civalleri, B., Ganguly, J., Perger, W.F., Belmonte, D., and Zuccolini, M.V. (2010) Thermo-chemical and thermo-physical properties of the high-pressure phase anhydrous B ($Mg_{14}Si_5O_{24}$): An ab-initio all-electron investigation. American Mineralogist, 95(4), 563–573.
Özgür, Ü., Alivov, Y.I., Liu, C., Teke, A., Reshchikov, M.A., Doğan, S., Avrutin, V., Cho, S.J., and Morko, H. (2005) A comprehensive review of ZnO materials and devices. Journal of Applied Physics, 98(4), 1–103.
Pankratz, L.B., and King, E.G. (1965) High-temperature heat contents and entropies of two zinc sulfides and four solid solutions of zinc and iron sulfides. U.S. Bureau of Mines, 6708.
Parlinski, K., Li, Z.Q., and Kawazoe, Y. (1997) First-principles determination of the soft mode in cubic ZrO_2. Physical Review Letters, 78(21), 4063–4066.
Pascale, F., Zicovich-Wilson, C.M., Gejo, F.L., Civalleri, B., Orlando, R., and Dovesi, R. (2004) The calculation of the vibrational frequencies of crystalline compounds and its implementation in the CRYSTAL code. Journal of Computational Chemistry, 25(6), 888–897.
Peintinger, M.F., Oliveira, D.V., and Bredow, T. (2013) Consistent gaussian basis sets of Triple-Zeta valence with polarization quality for solid-State Calculations. Journal of Computational Chemistry, 34(6), 451–459.
Perdew, J.P., Burke, K., and Ernzerhof, M. (1996) Generalized gradient approximation made simple. Physical Review Letters, 77(18), 3865–3868.
Perger, W.F. (2010) First-principles calculation of second-order elastic constants and equations of state for lithium azide, LiN_3, and lead azide, $Pb(N_3)_2$. International Journal of Quantum Chemistry, 110(10), 1916–1922.
Perger, W.F., Criswell, J., Civalleri, B., and Dovesi, R. (2009) Ab-initio calculation of elastic constants of crystalline systems with the CRYSTAL code. Computer Physics Communications, 180(10), 1753–1759.
Prencipe, M., Scanavino, I., Nestola, F., Merlini, M., Civalleri, B., Bruno, M., and Dovesi, R. (2011) High-pressure thermo-elastic properties of beryl ($Al_4Be_6Si_{12}O_{36}$) from ab initio calculations, and observations about the source of thermal expansion. Physics and Chemistry of Minerals, 38(3), 223–239.
Robie, R.A., and Hemingway, B.S. (1995) Thermodynamic properties of minerals and related substances at 298.15 K and 1 bar (10^5 Pascals) pressures and at higher temperatures. U.S. Geological Survey Bulletin 2131. U.S. Geological Survey, Denver, Colorado.
Sang, L., Liao, M., and Sumiya, M. (2013) A comprehensive review of semiconductor ultraviolet photodetectors: From thin film to one-dimensional nanostructures. Sensors (Switzerland), 13(8), 10482–10518.
Sharma, M., Mishra, D., and Kumar, J. (2019) First-principles study of the structural and electronic properties of bulk ZnS and small ZnnSn nanoclusters in the framework of the DFT plus U method. Physical Review B, 100(4), 12.
Sinha, T., Lilhare, D., and Khare, A. (2018) Effects of various parameters on structural and optical properties of CBD-grown ZnS thin films: A review. Journal of Electronic Materials, 47(2), 1730–1751.
Stuve, J.M. (1974) Low-temperature heat capacities of sphalerite and wurtzite, 7940. U.S. Bureau of Mines.
Togo, A., and Tanaka, I. (2015) First principles phonon calculations in materials science. Scripta Materialia, 108, 1–5.
Uchida, N., and Saito, S. (1972) Elastic and photoelastic constants of α-ZnS. Journal of Applied Physics, 43(3), 971–976.
Ulian, G., and Valdrè, G. (2015a) Density functional investigation of the thermophysical and thermo-chemical properties of $2M_1$ muscovite. American Mineralogist, 100(4), 935–944.
——— (2015b) Density functional investigation of the thermophysical and thermochemical properties of talc $[Mg_3Si_4O_{10}(OH)_2]$. Physics and Chemistry of Minerals, 42(2), 151–162.
——— (2015c) Structural, vibrational and thermophysical properties of pyrophyllite by semi-empirical density functional modelling. Physics and Chemistry of Minerals, 42(7), 609–627.
——— (2017) Effects of fluorine content on the elastic behavior of topaz $Al_2SiO_4(F,OH)_2$. American Mineralogist, 102(1-2), 347–356.
——— (2018a) Anisotropy and directional elastic behavior data obtained from the second-order elastic constants of portlandite $Ca(OH)_2$ and brucite $Mg(OH)_2$. Data in Brief, 21, 1375–1380.
——— (2018b) Effect of mechanical stress on the Raman and Infrared bands of hydroxylapatite: a quantum mechanical first principle investigation. Journal of the Mechanical Behavior of Biomedical Materials, 77, 683–692.
——— (2018c) Second-order elastic constants of hexagonal hydroxylapatite ($P6_3$) from ab initio quantum mechanics: comparison between DFT functionals and basis sets. International Journal of Quantum Chemistry, 118(5), e25500.
——— (2018d) Equation of state of hexagonal hydroxylapatite ($P6_3$) as obtained from density functional theory simulations. International Journal of Quantum Chemistry, 118(12), e25553.
——— (2019a) Equation of state and second-order elastic constants of portlandite $Ca(OH)_2$ and brucite $Mg(OH)_2$. Physics and Chemistry of Minerals, 46(2), 101–117.
——— (2019b) Thermomechanical, electronic and thermodynamic properties of ZnS cubic polymorphs: an ab initio investigation on the zinc-blende–rock-salt phase transition. Acta Crystallographica, B75, 1042–1059.
Ulian, G., Tosoni, S., and Valdrè, G. (2014) The compressional behaviour and the mechanical properties of talc $[Mg_3Si_4O_{10}(OH)_2]$: a density functional theory investigation. Physics and Chemistry of Minerals, 41(8), 639–650.
Ulian, G., Moro, D., and Valdrè, G. (2018) First principle investigation of the mechanical properties of natural layered nanocomposite: Clinochlore as a model system for heterodesmic structures. Composite Structures, 202, 551–558.
Valdez, L.A., Caravaca, M.A., and Casali, R.A. (2019) Ab-initio study of elastic anisotropy, hardness and volumetric thermal expansion coefficient of ZnO, ZnS, ZnSe in wurtzite and zinc blende phases. Journal of Physics and Chemistry of Solids, 134, 245–254.
Wallace, D.W. (1998) Thermodynamics of Crystals. Dover Publications.
Wang, S.Q. (2006) First-principles study of the anisotropic thermal expansion of wurtzite ZnS. Applied Physics Letters, 88(6), 061902.
Wang, Y., Wang, J.J., Wang, W.Y., Mei, Z.G., Shang, S.L., Chen, L.Q., and Liu, Z.K. (2010) A mixed-space approach to first-principles calculations of phonon frequencies for polar materials. Journal of Physics: Condensed Matter, 22(20).
Wang, K., Xub, X., Ma, L., Wang, A., Wang, R., Luo, J., and Wen, S. (2017) Studies on triboluminescence emission characteristics of various kinds of bulk ZnS crystals. Journal of Luminescence, 186, 307–311.
Xu, Y.N., and Ching, W.Y. (1993) Electronic, optical, and structural properties of some wurtzite crystals. Physical Review B, 48(7), 4335–4351.
Xu, X., Li, S., Chen, J., Cai, S., Long, Z., and Fang, X. (2018) Design principles and material engineering of ZnS for optoelectronic devices and catalysis. Advanced Functional Materials, 28(36), 1802029.

Manuscript received October 18, 2019
Manuscript accepted February 2, 2020
Manuscript handled by G. Diego Gatta

Endnote:

[1]Deposit item AM-20-87330, CIF and Supplemental Material. Deposit items are free to all readers and found on the MSA website, via the specific issue's Table of Contents (go to http://www.minsocam.org/MSA/AmMin/TOC/2020/Aug2020_data/Aug2020_data.html).